IEEE Access
Multidisciplinary ⋮ Rapid Review ⋮ Open Access Journal

Received October 11, 2021, accepted November 11, 2021, date of publication November 18, 2021,
date of current version December 2, 2021.

Digital Object Identifier 10.1109/ACCESS.2021.3129266

Impact of PWM Voltage Waveforms on Magnet Wire Insulation Partial Discharge in SiC-Based Motor Drives

MOHAMED DIAB[1], (Senior Member, IEEE), WENZHI ZHOU[2], (Graduate Student Member, IEEE), CHRISTOPHER EMERSIC[3], XIBO YUAN[2], (Senior Member, IEEE), AND IAN COTTON[3], (Senior Member, IEEE)

[1]School of Mechanical, Electrical and Manufacturing Engineering, Loughborough University, Loughborough LE11 3TU, U.K.
[2]Department of Electrical and Electronic Engineering, University of Bristol, Bristol BS8 1TH, U.K.
[3]Department of Electrical and Electronic Engineering, University of Manchester, Manchester M13 9PL, U.K.

Corresponding author: Xibo Yuan (xibo.yuan@bristol.ac.uk)

This work was supported in part by U.K. EPSRC under Grant EP/S00081X/1.

ABSTRACT Partial discharge (PD) is a prime cause of premature failure of inverter-fed motor winding insulation. With the emergence of fast-switching wide-bandgap silicon-carbide (SiC) power semiconductor devices, random-wound motors are more vulnerable to highly repetitive PDs due to the high-frequency steep-fronted switching transitions that result in overvoltage oscillations at the motor terminals and non-uniform voltage distribution within the motor winding turns. This article investigates the impact of the applied PWM voltage waveforms on the PD behavior in SiC-based inverter-fed motors, including two-level, three-level, and quasi-three-level PWM waveforms. The electric field distribution inside insulation defects (air cavities) is analysed for the different PWM voltage waveforms to theoretically predict the number and phase of probable PD events within the fundamental cycle. An experimental PD measurement setup is used to validate the theoretical analysis by applying the PWM voltage waveforms, that are generated by SiC-based power converters, on a typical turn-to-turn motor winding insulation system created by a twisted pair of enamelled magnet wire. Phase-resolved PD patterns are generated to assess the PD behavior against the PWM characteristics of each voltage waveform and the associated overvoltage pattern when power cables are used to emulate the voltage reflections in cable-fed motor drives. Detailed experiment specifications are provided in this article involving PD measurement methods and PD data post-processing algorithms. The obtained results are assessed, and conclusions are drawn as a useful and timely reference that enhances the understanding of insulation PD process in SiC-based power electronics applications.

INDEX TERMS Inverter-fed motors, magnet wire insulation, motor overvoltage, partial discharge (PD), silicon carbide (SiC) devices, wide bandgap.

I. INTRODUCTION

Interest in decarbonising transport through electrification is growing to reduce the dependency on traditional fossil fuels and achieve higher efficiency and improved performance of transportation industry. While electric vehicles have already been commercialized, more-/all-electric aircrafts are currently a prioritized research endeavour [1]. The reachability of electrified mobility technologies has been further enhanced by the emergence of wide-bandgap power semiconductor devices, such as those based on silicon carbide (SiC) and gallium nitride (GaN) material, being attractive candidates for high power density motor drives with alleviated cooling requirements [2], [3]. However, the short switching transition times of SiC devices, which can be as little as tens of nanoseconds, result in a non-uniform voltage distribution within the winding turns of random-wound motors with peak voltage stress across the first few turns close to the terminals [4]. This overstress is further exacerbated when power cables are used to connect the inverter to the motor where the fast-switched PWM voltage pulses experience back and forth voltage reflections across the cables

The associate editor coordinating the review of this manuscript and approving it for publication was Zhehan Yi.

This work is licensed under a Creative Commons Attribution 4.0 License. For more information, see https://creativecommons.org/licenses/by/4.0/

resulting in motor terminal overvoltage that could reach twice the inverter voltage [5]. Although these challenging phenomena are invariably observed in traditional silicon-based inverter-fed motor drives [6], they become more pronounced and serious in the higher switching speed SiC-based counterparts. That is, the non-uniformity in voltage distribution across motor winding turns is strengthened while the motor terminal overvoltage is further stimulated at shorter cable lengths (e.g., few meters).

Sufficiently high-voltage levels across motor winding turns result in accelerated insulation ageing where the high motor turn-to-turn voltage can incept partial discharges (PDs) that progressively yield to the degradation of organic coatings of random-wound motor coils [7]. Since PD activity is fundamentally associated with electric field changes that exceed the PD inception field, there is a high probability of PD ignition at both flanks of each PWM voltage pulse. Thus, depending on the applied PWM voltage waveform, the PD repetition rate can be comparable to the PWM switching frequency. Since SiC power devices can operate at high switching frequencies, the consequent insulation degradation of a SiC inverter-fed motor, due to the highly repetitive PD activity, can lead to insulation failure in a short time by successively breaking the chemical bonds of the organic insulation [8].

Several studies have investigated the parameters affecting the PD behavior by applying repetitive square wave voltage pulses on a twisted pair of enamelled magnet wires [9]–[12]. These parameters include the frequency, rise time, pulse polarity, and duty cycle of the applied impulsive voltage. Although there is variability between studies on the detailed effects of these parameters on the PD behavior, they have a little impact on the PD inception voltage (PDIV) [13]. However, the rise time of the voltage pulse has the potential to indirectly promote the PD inception by the consequent overvoltage stress across the insulation winding due to the uneven voltage distribution between winding turns and the overvoltage oscillations due to power cables effect. Indeed, the PD is dominantly governed by the applied voltage magnitude and the associated electric field distribution inside the insulation cavities. Thus, analysing the PD behavior using repetitive square wave voltage pulses is not sufficiently representative for inverter-fed motors since the electric field distribution is substantially affected by the characteristics of the applied PWM voltage waveforms. Therefore, more contribution is needed to analyse the PD behavior within the fundamental cycle of the applied PWM voltage waveform, where PD inception depends not only on the PDIV level, but also on the aggregated electric field distribution. Furthermore, the impact of motor terminal overvoltage on PD behavior, under various PWM voltage waveforms, needs to be investigated since it has not been addressed in existing literature.

Though the research on PD has been mainly conducted by scholars in the field of high-voltage insulation and material, this article aims to enhance the understanding of PD inception mechanism from a power electronics point of view [14]. The contributions of this article can be summarized as follows:

- Presenting a tool to investigate the motor winding insulation PD within the fundamental cycle of applied PWM voltage waveforms.
- Predicting the number and phase location of probable PD events within the fundamental cycle of applied PWM voltage waveforms.
- Analysing the PD behavior of four typical PWM voltage waveforms applicable to motor drives, namely, unipolar two-level (2L), bipolar 2L, three-level (3L), and quasi-three-level (Q3L), considering the impact of consequent motor terminal overvoltage, due to voltage reflection through power cables, on winding insulation PD.
- Providing a useful and timely knowledge for power electronics engineers to select suitable PWM schemes and system architectures for motor drives and assess the reliability of overvoltage mitigation methods to prevent PD activities in SiC-based inverter-fed motors.

The theoretical PD investigation presented in this article is verified through experimental data analysis, where statistical phase-resolved PD (PRPD) patterns are generated to assess the PD behavior of employed PWM voltage waveforms.

The remainder of this article is organized as follows. Section II revisits the characteristics of assessed PWM voltage waveforms and the consequent overvoltage oscillations when propagating through power cables. Section III theoretically investigates the PD behavior of the PWM voltage waveforms based on the electric field distribution inside the insulation cavities. Section IV presents the experimental setup specifications to generate the PWM voltage waveforms and measure the PD in a twisted pair of magnet wires. Section V illustrates the PD data post-processing and detection algorithms to generate PD statistics. Section VI provides remarks while Section VII concludes the article findings and contributions.

II. PWM VOLTAGE WAVEFORMS AND CONSEQUENT OVERVOLTAGE

Industrial motors are usually powered by voltage-source inverters (VSIs) that can provide speed and/or torque control. Motor drives are commonly implemented using 2L and 3L VSIs, where the sinusoidal PWM technique or the space vector modulation can be adopted to generate the driving signals of employed switching devices [15]. When the switched PWM voltage pulses travel from the inverter to the motor through power cables, they experience successive voltage reflections due to the impedance mismatch between the cable and the motor. This results in a motor overvoltage that is quantified depending on the relation between the voltage pulse rise time t_r and the wave propagation time t_p which depends on the cable length. When the pulse rise time is significantly shorter than triple the wave propagation time (i.e., $t_r \ll 3t_p$), the motor voltage can experience full voltage reflection where the motor voltage is doubled compared to the inverter voltage [16]. With fast-switching SiC power devices, the voltage doubling effect can be stimulated at shorter cable lengths than those utilized when silicon devices are employed.

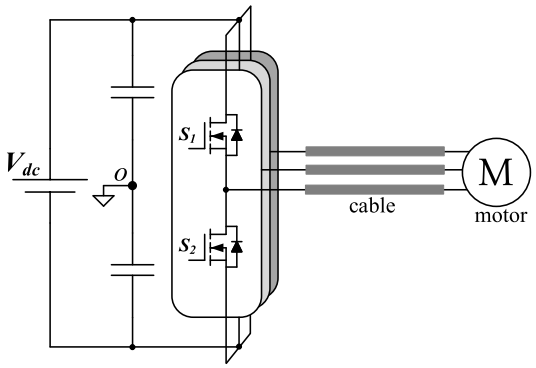

FIGURE 1. Circuit diagram of 2L VSI supplying a three-phase motor through power cables.

It should be noted that the peak motor voltage varies depending on the characteristics of the inverter PWM voltage waveform, where the voltage doubling effect does not necessarily mean the motor peak voltage is always twice the dc-link voltage. This is elaborated in the next subsections where the different PWM schemes that can be applied to the 2L and 3L VSIs are briefly revisited while consequent overvoltage oscillation patterns when the generated PWM voltage waveforms propagate through power cables are demonstrated.

A. 2L CONVERTER MODULATION

The 2L converter is a widespread VSI topology that has been adopted in many diversified applications. It is schematically shown in Fig. 1 supplying a three-phase motor through power cables. The 2L VSI is commonly modulated using either the unipolar or bipolar sinusoidal PWM scheme. In the unipolar PWM scheme, the voltage pulses have the same polarity as the equivalent sinusoidal waveform. Whereas, in the bipolar PWM scheme (which is applicable to single-phase VSIs or three-phase dual VSIs for open-ended winding machines), the voltage pulses alternate between the two pole voltages (i.e., $-V_{dc}$ and V_{dc}) within the entire fundamental cycle.

Fig. 2 shows the propagation of unipolar and bipolar 2L PWM voltage waveforms when travelling through power cables with the critical length which causes the voltage doubling effect, where the rise time of the voltage pulses is much shorter than triple the wave propagation time. In Fig. 2a, the unipolar voltage pulses, throughout the positive half cycle, ramp from 0 to V_{dc} within a rise time t_r and experience full voltage reflection when arriving at the motor side. Thus, the V_{dc} voltage surge is reflected towards the inverter side resulting in a peak motor voltage of $2V_{dc}$. The same scenario occurs for the voltage pulses in the negative half cycle. On the other side, the bipolar voltage pulses ramp from $-V_{dc}$ to V_{dc} within a rise time t_r, that is, the voltage surge at the inverter side is $2V_{dc}$. When this voltage surge propagates through the power cable, it experiences a full voltage reflection at the motor side, resulting in $4V_{dc}$ voltage variation at the motor terminals. Thus, the motor peak voltage is $3V_{dc}$ since the motor voltage originally alternates from $-V_{dc}$ during the rising voltage transition, as shown in Fig. 2b. The same voltage

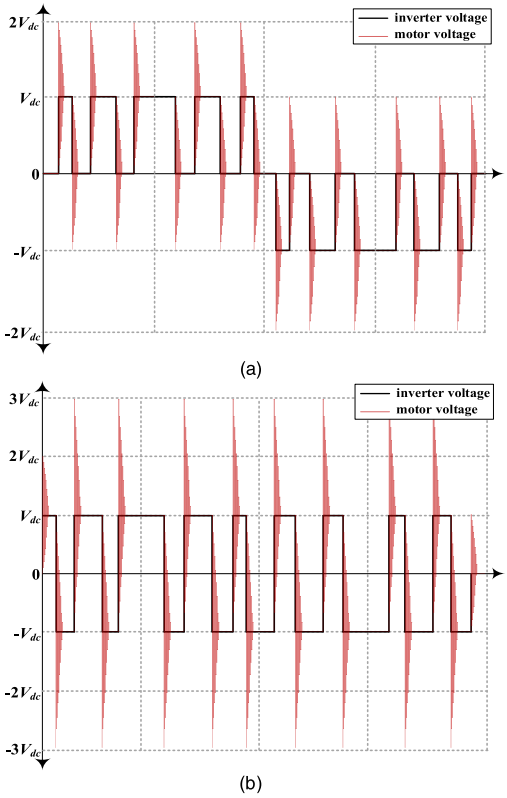

FIGURE 2. Overvoltage oscillations of 2L VSI, when the output voltage waveform travels through power cables with critical length, using (a) unipolar PWM scheme and (b) bipolar PWM scheme (for single-phase or dual VSI topologies).

reflection mechanism occurs during the falling transitions of the bipolar voltage pulses.

B. 3L CONVERTER MODULATION

3L converters can be used as a feasible replacement for 2L converters with enhanced efficiency and lower output voltage harmonics [15]. The T-type converter is a simple example that can be used to generate a 3L voltage waveform. It inherits the structure of standard 2L converters, however, with auxiliary branches connecting the dc-link midpoint to the output nodes of each phase leg. The auxiliary branches are realized using a bidirectional switch that is commonly implemented via a pair of switching devices in common-source configuration. Since the bidirectional switch only needs to block half the dc-link voltage, the auxiliary switching devices are rated at $0.5V_{dc}$ [17]. The T-type converter is schematically presented in Fig. 3, where power cables are used to connect the converter to a three-phase motor.

When a 3L converter is used in cable-fed motor drives, the output voltage still experiences voltage reflection since the voltage waveform is pulse modulated. However, the peak motor voltage is quantified by the overvoltage associated with the highest voltage level during the modulation cycle, where other lower voltage levels experience overvoltage that is always lower than V_{dc} (i.e., lower than the inverter rated voltage). This is elucidated in Fig. 4a, where the motor

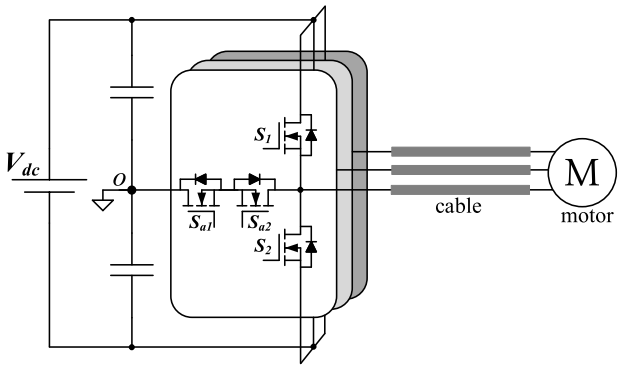

FIGURE 3. Circuit diagram of T-type VSI supplying a three-phase motor through power cables.

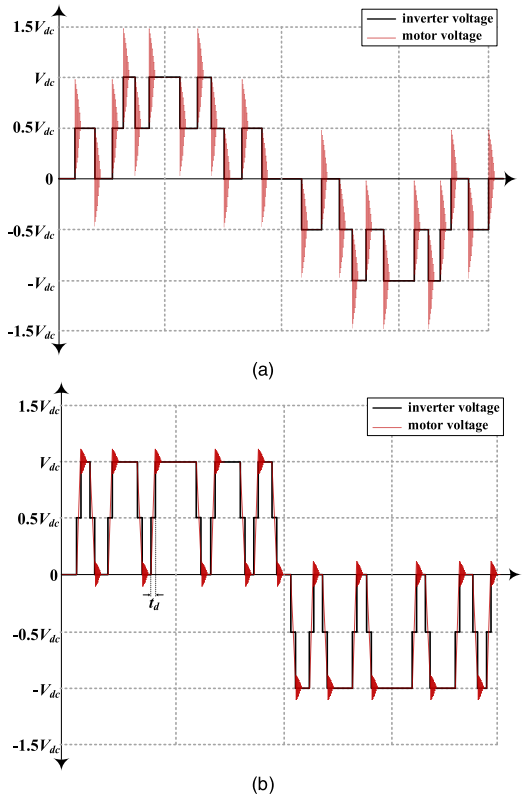

FIGURE 4. Overvoltage oscillations of T-type converter, when the output voltage waveform travels through power cables with critical length, using (a) 3L PWM scheme and (b) Q3L PWM scheme.

voltage experiences overvoltage oscillations, due to the cable effect, with a peak voltage limited to 1.5 times the inverter rated voltage (i.e., the peak motor voltage is $1.5V_{dc}$ at most).

As an alternative to the 3L modulation, Q3L modulation has been adopted to mitigate the motor overvoltage in cable-fed motor drives [18]. The key idea of the Q3L approach is reshaping the PWM voltage transition pattern based on the observation that the voltage reflection across the cables can be cancelled by splitting the rising and falling transitions of the 2L PWM voltage pulses into two identical voltage steps with an appropriate separation time. In the midst

TABLE 1. A comparison between PWM voltage waveforms.

Waveform	Unipolar 2L	Bipolar 2L	3L	Q3L
Voltage surge (ΔV) per switching transition	V_{dc}	$2V_{dc}$	$0.5V_{dc}$	V_{dc}
Maximum overvoltage	$2V_{dc}$	$3V_{dc}$	$1.5V_{dc}$	$1.2V_{dc}$

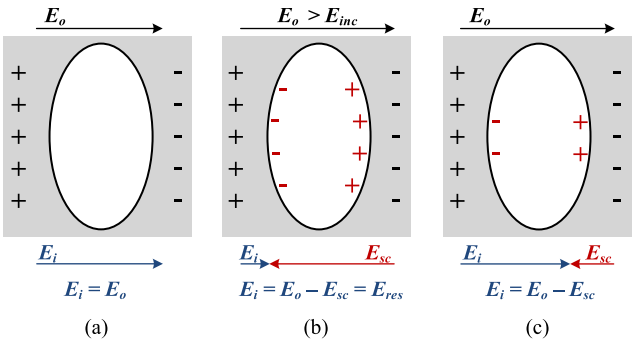

FIGURE 5. Electric field distribution inside an insulation cavity (a) before a PD, (b) immediately after a PD, and (c) after a PD while.

of the split voltage transition, an intermediate voltage level is temporarily adopted, as shown in Fig. 4b. The delay time separating the two switched voltage steps is referred to as the dwell time t_d which is set as twice the wave propagation time (i.e., $t_d = 2t_p$). This allows the voltage reflection of the first voltage step to be significantly counterbalanced by the incidence of the second voltage step, as detailed in [19], with a 20% motor overvoltage at most. The resultant motor voltage has a 2L waveform crossing the inverter Q3L voltage waveform at the dwell time midway, as presented in Fig. 4b. It is worth mentioning that compared to a standard 3L T-type converter, the Q3L modulation requires lower current rating of the auxiliary switching devices since they only conduct during the short dwell time intervals.

A summarized comparison between the four PWM voltage waveforms in terms of the voltage surge (ΔV) in each switching transition and the maximum associated overvoltage during propagation through power cables is shown in Table 1.

III. PARTIAL DISCHARGE INCEPTION AND ELECTRIC FIELD DISTRIBUTION

The PD inception process has been illustrated in several articles in literature [20], [21]. A brief characterization for this process is given in this section with graphical demonstration as shown in Fig. 5. Starting with a PD-free insulation cavity, as shown in Fig. 5a, the internal field E_i inside the cavity is only maintained by the external field E_o which is directly proportional to the applied voltage at the system electrodes. If a starting electron is available to incept electronic avalanche and the internal electric field exceeds the inception field E_{inc} which corresponds to the PDIV, a charge is transferred across the cavity surface (i.e., PD occurs). The deposited space charge creates a counter field E_{sc} that opposes the internal field, as envisaged in Fig. 5b, leaving a reduced

residual net field E_{res}. This residual field strength is below the inception field; thus, no further PD occurs. As time elapses, the cavity surface charge starts to migrate and recombine along the insulation surface decreasing the space charge field, where the internal field gradually recovers approaching the external field level, as depicted in Fig. 5c. When the internal field strength again exceeds the inception field strength, with availability of a free electron, PD inception can reoccur.

The PD behavior of a given PWM voltage waveform can be examined by sketching the internal electric field distribution inside the insulation air cavities within the fundamental cycle. It should be noted that two assumptions are considered in the field distribution diagrams: 1) there is an infinite availability of free electrons at each impulsive voltage flank to start electronic avalanche and 2) the space charge recombination rate is much slower than the switching frequency of the PWM voltage waveform (i.e., long memory effect). In the following subsections, the PD behavior and electric field distribution are presented for each of the four PWM voltage waveforms analysed in Section II.

A. UNIPOLAR 2L PWM VOLTAGE WAVEFORM

For a unipolar 2L PWM voltage waveform, two field distribution diagrams are sketched in Fig. 6 to show how the PD behavior is affected by the waveform characteristics and the consequent overvoltage pattern when the cable effect is considered. Fig. 6a shows the electric field distribution of the unipolar 2L waveform when the external applied field magnitude (E_p) is slightly higher than the inception field (the PDIV). Starting with the negative half cycle, the internal field initially equals the external applied field, thus the first voltage pulse can trigger a PD event at its rising transition from 0 to $-V_{dc}$ (marked as event 0) since the internal field exceeds the PDIV level. The resultant space charge field drops the internal field to the negative residual field level ($-E_{res}$). The space charge field prevents further PDs to be incepted at the next impulsive voltage flanks within the negative half cycle, where the internal field is always limited to $E_p - E_{res}$ which is lower than the PDIV level. At the negative-to-positive polarity reversal, a PD event (marked as event 1) can be triggered by the aggregated electric field strength ($2E_p - E_{res}$). Following this PD event, no further PDs can be incepted at the next impulsive voltage flanks within the positive half cycle. At the positive-to-negative polarity reversal, another PD event (marked as event 2) can be incepted in a similar way of PD event 1. Therefore, two PD events can be observed within the fundamental cycle of the unipolar 2L waveform at the two polarity reversal instants, if an initial PD event is triggered (i.e., PD event 0) at any prior time instant.

When the unipolar 2L waveform propagates through power cables in inverter-fed motor drives, it experiences voltage reflection where the peak motor voltage can be twice the inverter voltage. Fig. 6b emulates the overvoltage effect on the PD behavior of the unipolar 2L waveform where the external applied field is significantly higher than the PDIV

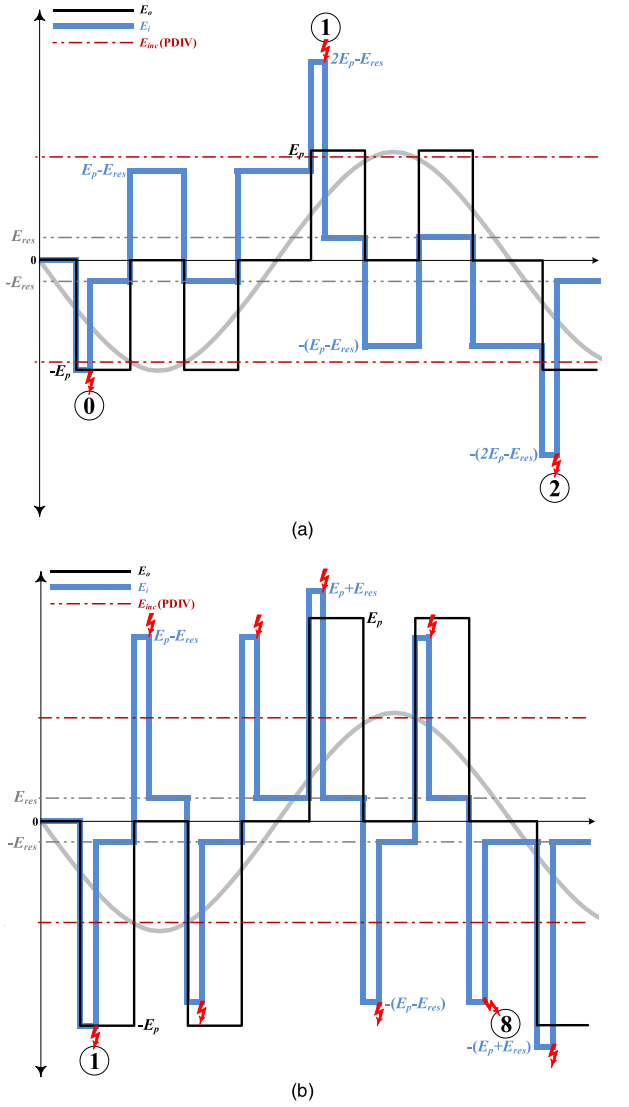

FIGURE 6. Electric field distribution inside an insulation cavity under unipolar 2L PWM voltage waveform when the external applied field is: (a) slightly higher than the PDIV (b) significantly higher than the PDIV.

level. Thus, PD events can be incepted at both flanks of each voltage pulse, where the probable number of PDs can be double the number of the voltage pulses within the fundamental cycle (e.g., 8 PDs are observed in Fig. 6b for 4 unipolar pulses per fundamental cycle).

B. BIPOLAR 2L PWM VOLTAGE WAVEFORM

Fig. 7 shows the PD behavior of the bipolar 2L PWM voltage waveform when it has the same voltage magnitude as the unipolar 2L waveform shown in Fig. 6a (i.e., the same operating dc-link voltage). Since there is a polarity reversal at each voltage transition, PDs can be incepted at all voltage flanks in the fundamental cycle where the internal electric field is amplified in the same direction of the space charge field of the prior PD event.

When the bipolar 2L waveform experiences voltage reflection due to the cable effect, the motor peak voltage will be

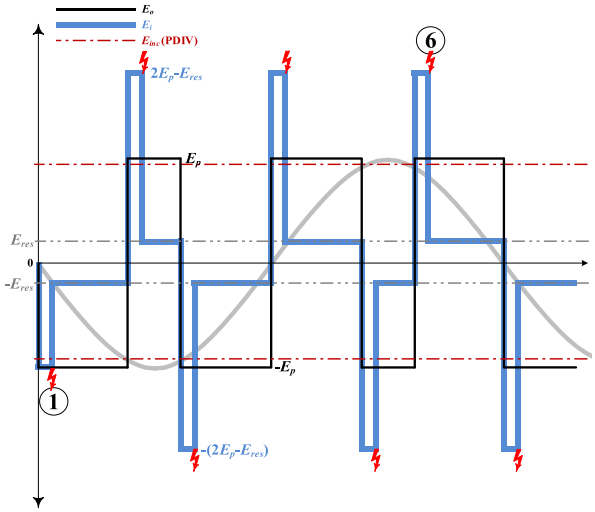

FIGURE 7. Electric field distribution inside an insulation cavity under bipolar 2L PWM voltage waveform.

overrated as previously shown in Fig. 2b. Thus, the external applied field due to the overvoltage oscillations will be significantly higher than the PDIV level. This considerably increases the probability of PD inception at both flanks of each voltage pulse, in the same way illustrated in Fig. 7, however with magnified PD amplitudes.

C. 3L PWM VOLTAGE WAVEFORM

Fig. 8a presents the PD behavior of the 3L PWM voltage waveform in a fundamental cycle when the dc-link voltage is slightly higher than the PDIV (i.e., E_p is slightly higher than E_{inc}). Starting with the negative half cycle, the internal field exactly follows the external applied field which is lower than the PDIV level when the waveform is switched from 0 to $-0.5V_{dc}$. At the first traverse of the waveform from $-0.5V_{dc}$ to $-V_{dc}$, the internal field exceeds the PDIV level where a PD event can be incepted (event 1). Subsequently, the internal field has several rising and falling alternations between different field levels that are lower than the PDIV. At the negative-to-positive polarity reversal, the internal field is aggregated exceeding the PDIV level where a PD event can be incepted (event 2) and the internal field is then dropped to the positive residual field level (E_{res}). This prevents further PDs to be incepted in the remainder of the fundamental cycle. Therefore, two PD events are probable in the fundamental cycle of the 3L waveform, with the phase locations envisaged in Fig. 8a.

The PD behavior of the 3L PWM waveform with superimposed overvoltage oscillations due to cable effect is shown in Fig. 8b. The external electric field associated with the overvoltage oscillations during switching from 0V to the first voltage level (i.e., $\pm 0.5V_{dc}$) is considered slightly lower than the PDIV level, while the electric field associated with the overvoltage oscillations during switching from the first to the second voltage level (i.e., from $\pm 0.5V_{dc}$ to $\pm V_{dc}$) is much higher than the PDIV. Accordingly, six PD events can be

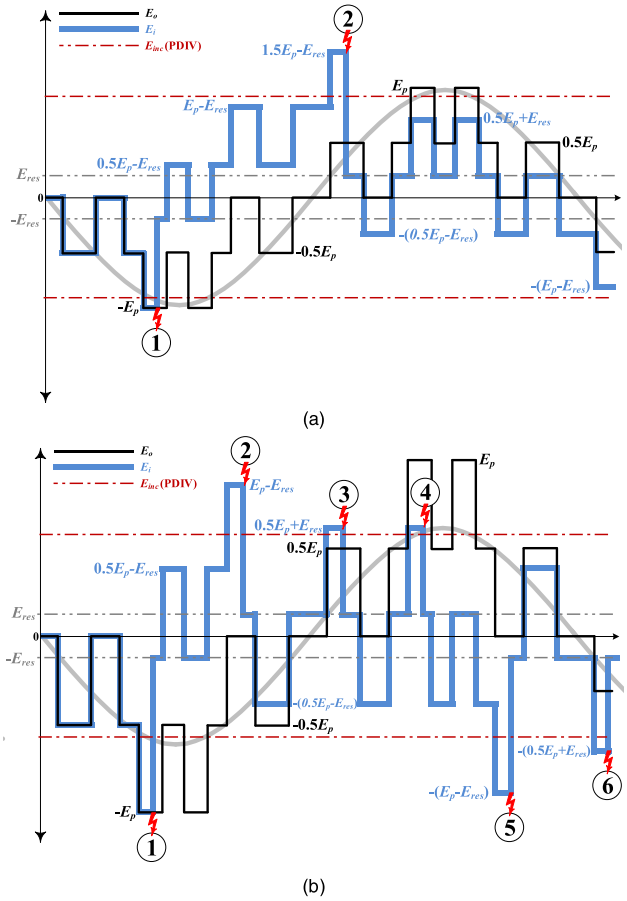

FIGURE 8. Electric field distribution inside an insulation cavity under 3L PWM voltage waveform when the peak external applied field is (a) slightly higher than the PDIV (b) significantly higher than the PDIV.

incepted within the fundamental cycle when the internal electric field is exacerbated beyond the PDIV level. This occurs at the polarity reversal instants of the fundamental cycle, the first rising transition from the first voltage level to the second one in each half cycle, and the last falling transition from the second voltage level to the first one in each half cycle, as elucidated in Fig. 8b.

D. Q3L PWM VOLTAGE WAVEFORM

The PD behavior of the Q3L PWM voltage waveform can only be studied when the cable effect is considered, where the Q3L waveform is advantageous in mitigating the motor overvoltage oscillations. Since a Q3L inverter voltage with optimal dwell time results in a 2L motor voltage with 20% overvoltage oscillations at most, the PD behavior of the Q3L waveform can be comparable to that of a unipolar 2L waveform. Therefore, if the PDIV level is slightly lower than the external applied field, PD events are probable only at the polarity reversal time instants of the waveform, as exemplified in Fig. 6a. Whereas, when the PDIV level is much lower than the peak applied field, some PD events can be incepted at any of the voltage transitions within the fundamental cycle, in addition to the polarity reversal PDs.

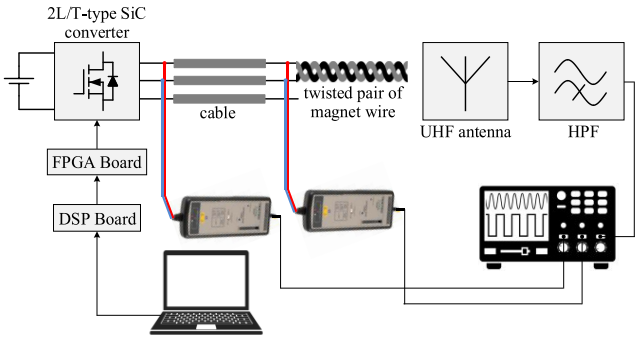

FIGURE 9. Schematic diagram of the experimental PD setup.

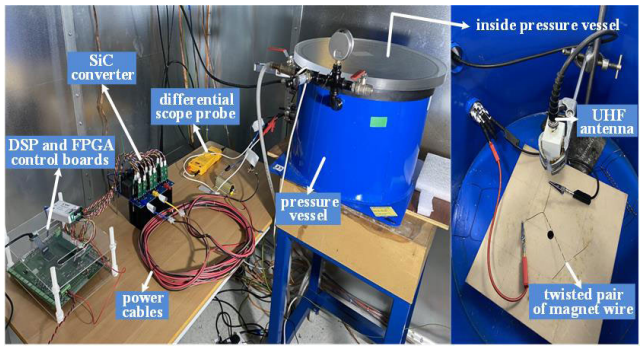

FIGURE 10. Hardware view of the experimental PD setup.

A conclusive remark can be drawn from previous field distribution diagrams that the voltage jump (ΔV) of the applied PWM waveform, or the consequent overvoltage, is the key factor determining the PD occurrence. The 3L waveform has the lowest PWM voltage jump compared to other addressed waveforms. Whereas, the 3L and Q3L waveforms have the lowest associated overvoltage jump compared to the unipolar and bipolar 2L waveforms.

IV. EXPERIMENTAL PD MEASUREMENT SETUP

A PD measurement setup has been used to practically assess the PD behavior of the analysed PWM voltage waveforms. Fig. 9 shows a schematic diagram of the implemented setup, while Fig. 10 shows hardware view of the main components utilized in the experiment. A standard 2L converter was used to generate single-phase unipolar and bipolar 2L PWM voltage waveforms, while a T-type converter was used to generate single-phase 3L and Q3L PWM voltage waveforms. Both converters are based on C2M0040120D SiC power MOSFETs driven by gate drivers with 25Ω gate resistance where the switching rise/fall time is 50ns. The converters were fed through a 600V dc-link power supply, switched at 40kHz, and controlled using DSP (TI TMS320F28335) and FPGA (Xilinx XC3S400) boards. A three-core 12m long 12 AWG PVC cable was used to emulate the voltage reflections in cable-fed motors. A twisted pair of magnet wires (one enamelled and one bared) was used as a test sample to simulate a typical turn-to-turn motor winding insulation system. The magnet wire is 24.5 AWG with 24μm enamel coating thickness. The sample was placed inside a controlled pressure vessel, where the pressure has been maintained constant at 650mbar during the entire experiment to reduce the PDIV level and promote the PD occurrence. This also emulates the operating conditions of aerospace applications (e.g., more-electric aircrafts) where the pressure is lower than the atmospheric pressure. The ambient temperature during measurements was in the range of 17.5–19.5°C while the dew point temperature was 4.3°C. An ultra-high frequency (UHF) antenna was used as an electromagnetic sensor to measure the PD amplitude. The antenna was directly facing the test sample and has been maintained in a fixed position with respect to the test sample to avoid any possible influence of the setup arrangement on the obtained PD results. To avoid interference between the PD signal and the switching noise associated with the commutation of the SiC power devices, the antenna output was connected to a high-pass filter with 600–3000 MHz bandwidth. This was selected based on the observation that the PD phenomenon usually generates signals that fall in the UHF band (300–3000 MHz) while the switching interference mainly contains frequency components with much lower frequency spectrum. The filter output was attached to a 1GHz bandwidth, 10Gs/s digital oscilloscope (Lecroy WaveRunner 104Xi). The voltages across the inverter terminals and the test sample terminals were measured using high voltage and bandwidth differential voltage probes. The cables connecting the measured voltages to the oscilloscope have the same 50Ω resistance as the oscilloscope internal channels to eliminate any impedance mismatch in the measurement setup. The experiment was conducted in a Faraday cage to reduce the background electrical noise and maximise low-amplitude PD detection.

Two experimental scenarios were considered for the PD measurement of the different PWM voltage waveforms. In the first scenario, the inverter output voltage was directly connected to the test sample. Whereas, in the second scenario, the 12m power cables were connected between the inverter and the test sample to produce overvoltage oscillations at the sample terminals to promote the PD inception. During the experiment, the inverter and test sample voltages along with the antenna output voltage were continuously recorded for 100 times in a pre-fixed time range (a fundamental cycle of the applied voltage waveform) to obtain a large statistical PD dataset for each voltage waveform in each operating scenario. To reduce the size of recorded data in the oscilloscope internal memory, the fundamental frequency of the applied PWM voltage waveforms was 1kHz.

To quantify the frequency contents of the background electromagnetic noise, an initial test was performed at 300V using unipolar impulsive voltages without connecting neither the sample nor the high-pass filter. This is demonstrated in Fig. 11a where the voltage at the inverter terminals and at the cable-end terminals are shown along with the antenna output. A significant noise (up to 130mV) can be noticed at both rising and falling switching transitions of the voltage

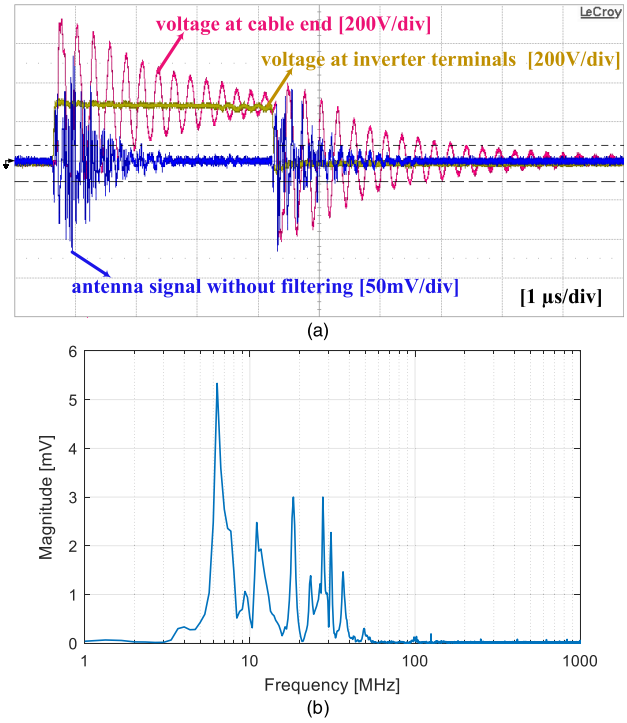

FIGURE 11. Background noise due to the commutation of switching devices, in (a) time domain and (b) frequency domain.

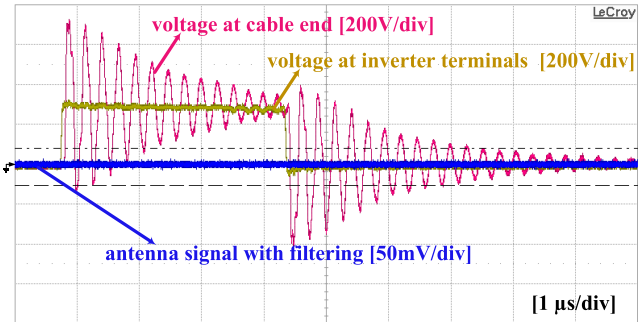

FIGURE 12. Attenuated background noise due to utilization of high-pass filter.

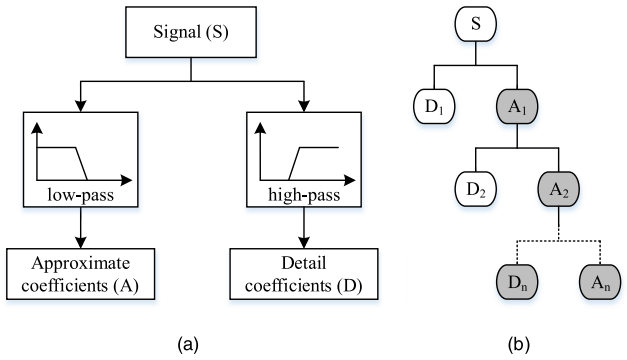

FIGURE 13. Wavelet decomposition flowchart: (a) complementary filtering action and (b) iterative decomposition levels.

pulse due to the commutation of the semiconductor devices. As shown in Fig. 11b, the frequency spectrum of the switching noise is limited to 60MHz. When the filter was connected in cascade with the antenna output, the switching noise was significantly attenuated, as evidenced in Fig. 12, since its frequency components are lower than the band-pass of the employed filter.

All equipment of the experimental setup have been verified PD free (i.e., no PD is incepted elsewhere in the test setup) by performing another test at 600V, without connecting the test sample. The antenna output signal has been within the normal parasitic level of background noise.

V. PD DATA PROCESSING AND STATISTICS

Although the high-pass filter utilization is effective to reject the dominant electromagnetic switching noise interfered with the antenna output, the PD signal can still be masked with the remaining embedded background noise. Therefore, a post-processing of the antenna's output signal is adopted for signal denoising and automated PD recognition. This is essential to generate PRPD patterns that are the most common format to interpret the PD measurement results providing information about PD distribution in relation to the applied voltage waveform [22].

A. PD DATA PROCESSING

Several denoising techniques, either in time or frequency domain, can be adopted for PD signal extraction. Among them, the wavelet decomposition is a powerful tool in denoising PD signals, where the resulting high-frequency signal becomes much smoother allowing easy PD signal extraction [23]. The wavelet decomposition process works as complementary low-pass and high-pass filters that decouple the original signal (S) into a series of approximate (A) and detail (D) coefficients, respectively, as shown in Fig. 13a [24]. Through iterative procedure, the approximate coefficients are used as the new input for the next decomposition level, as schematically shown in Fig. 13b, where the subscript 'n' is the number of decomposition levels. The output signal of the wavelet decomposition process comprises the last generated detail coefficients in addition to the sum of all generated approximate coefficients (i.e., the sum of grey-highlighted blocks in Fig. 13b). Fig. 14 shows an example of a denoised antenna signal using the wavelet decomposition approach where the high-frequency components of the background noise have been significantly attenuated allowing easier dissociation of PD signatures without altering the PD signal quality.

For a fully automated PD detection within the fundamental cycle of the applied PWM voltage waveform, a PD detection algorithm has been implemented by splitting the PWM waveform into subdivisions where each subdivision encompasses the region between each two successive voltage flanks. Through an iterative process, the denoised antenna signal is screened in each subdivision to look for PDs. To be recognized as a PD, the detected signal should be large enough to be considered as something other than just a random noise. As a rule of thumb, the peak of the denoised signal should

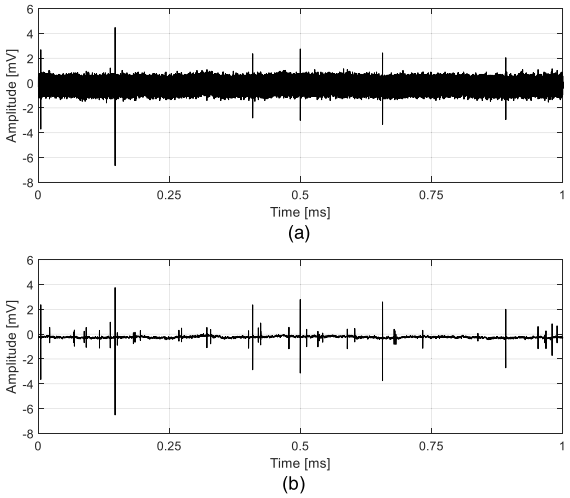

FIGURE 14. Antenna signal (a) before denoising and (b) after denoising using wavelet decomposition.

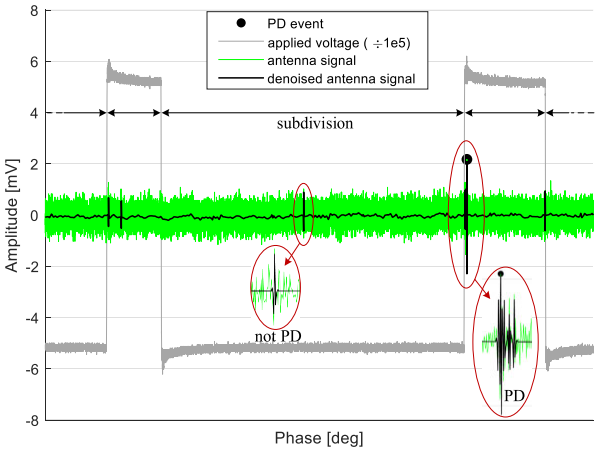

FIGURE 15. Example of PD discrimination from random impulsive noise.

be larger than twice the average of the background noise envelope to be considered as a true PD event. When this condition is verified, the PD amplitude and phase are saved, and the screening process continues to the next subdivision. Fig. 15 shows an example of the PD detection algorithm, where bipolar PWM voltage pulses are split into subdivisions to look for PDs in between. Importantly, not all detected spikes in the subdivisions are considered PDs where the PD condition is only verified in one impulsive event, while other detected spikes are just random impulsive noise.

B. PRPD PATTERNS

PRPD patterns have been generated by running the experiment under the different PWM voltage waveforms while processing the collected data using the previously presented algorithms. The experiment procedure implies increasing the dc-link voltage gradually until PD initiates, where the operating voltage level is then recorded as the dc-link inception voltage.

Starting with the unipolar 2L PWM waveform, the PD onset has been recorded at a dc-link voltage of 470V when the inverter voltage is directly applied to the sample without connection cables (i.e., PDIV = 470V). Fig. 16a shows the PD distribution relative to the fundamental cycle of the unipolar 2L waveform at 500V. Since the applied voltage is slightly higher than the PDIV level, PD events are stationed only at the polarity reversal instants of the waveform where the incepted PDs at these time instants prevent further PDs to be incepted at other voltage pulses within the fundamental cycle, as previously illustrated in Fig. 6a. When the 12m cable, which is longer than the critical cable length, was connected between the inverter and the sample, significant overvoltage oscillations resulted at the sample terminals (almost double the inverter voltage). The PD onset was recorded at a dc-link voltage of 300V where the peak sample voltage was 600V. The PRPD pattern for the cable-connected scenario of the unipolar 2L waveform is shown in Fig. 16b at 500V (i.e., the peak sample voltage is around 1000V). Since the peak sample voltage is much higher than the PDIV level, intense PD activity is observed at all voltage transitions within the fundamental cycle, where the electric field distribution inside the sample insulation cavities offers almost an equal probability of PD inception at all voltage transitions, as previously elaborated in Fig. 6b.

Considering the bipolar 2L PWM waveform, the PDIV level has been recorded at 490V when the inverter voltage is directly applied to the sample. Fig. 17a shows the PD distribution within the fundamental cycle of the bipolar 2L waveform at 500V (slightly higher than the PDIV). It can be noticed that most of the voltage transitions have many associated PD events. However, less/no PD activity can be observed at some PWM voltage transitions, within the positive half cycle, that have larger duty cycles. When the overvoltage oscillations are stimulated by connecting power cables between the inverter and the sample, the PD onset was observed at 187V dc-link voltage. It should be noted that at this dc-link voltage, the peak sample voltage is around 561V since the maximum overvoltage for bipolar 2L waveform is $3V_{dc}$. This results in much intense PD activity (in amplitude and repetition rate) across all voltage transitions, as shown in the PRPD pattern in Fig. 17b. This returns to the significantly high voltage slew-rate (dv/dt) of the overvoltage oscillations where they exceed the PDIV level in a very short time. Published research shows that although the rise time does not have a significant impact on the PDIV level, it can affect the resultant PD magnitude [9]. That is, the shorter the time at which the applied voltage pulse exceeds the PDIV level, the larger the resultant PD magnitude with a predominance of high frequency components in the energy spectrum.

When the 3L PWM voltage waveform is directly applied to the test sample, the PDIV was recorded at 480V. Fig. 18a shows the PRPD distribution of the 3L PWM waveform at 600V. Several PD events are detected at the transition from −300V to −600V, whereas very limited PDs are observed at the transition from 300V to 600V. This partially

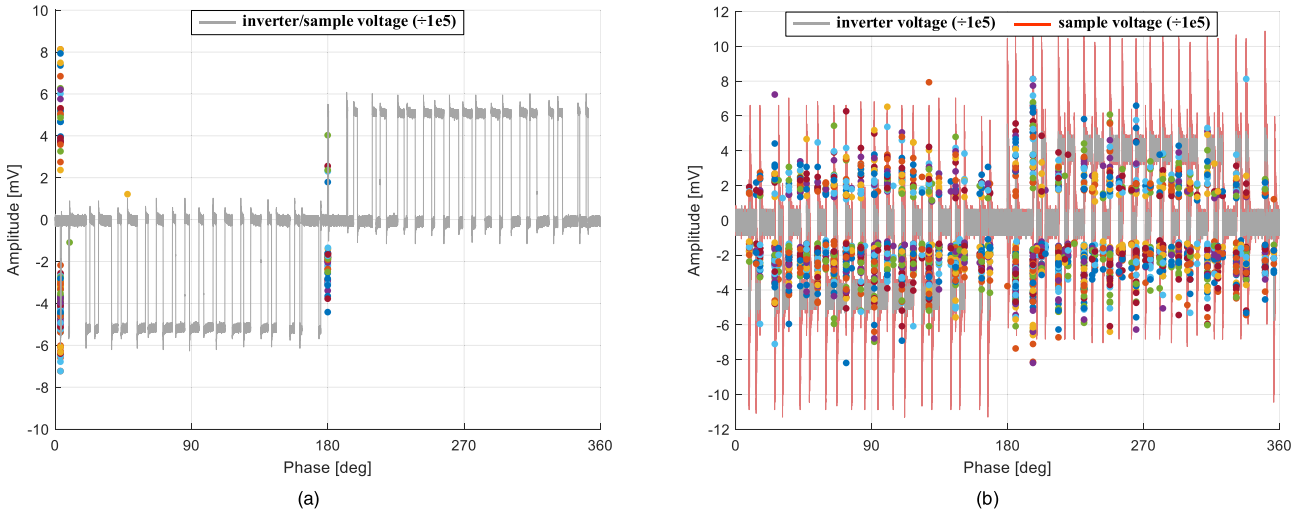

FIGURE 16. PRPD patterns for unipolar 2L PWM voltage waveform at 500V (a) without cable connection (b) with cable connection.

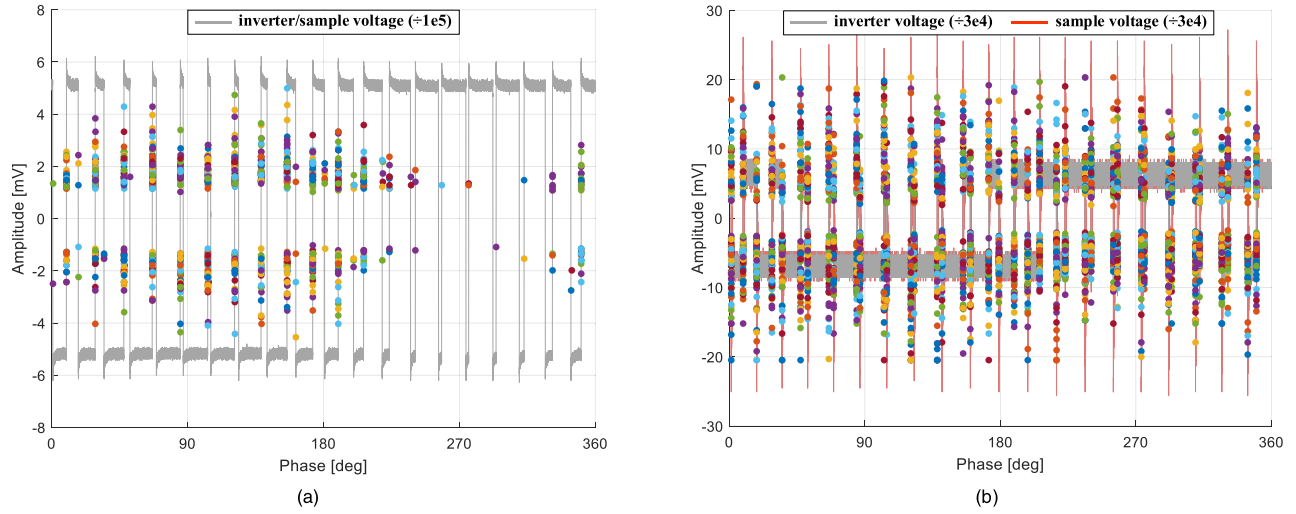

FIGURE 17. PRPD patterns for bipolar 2L PWM voltage waveform (a) without cable connection at 500V (b) with cable connection at 187V.

agrees with the theoretical analysis in Fig. 8a which also predicts PD events to be incepted at the negative-to-positive polarity reversal. However, since Fig. 8a is sketched based on the assumption that the insulation cavities have a long memory effect, probably this assumption has not met true for this specific experimental case study of the 3L PWM waveform. That is, the space charge recombination time is not significantly longer than the PWM switching cycle where the space charge field can vanish and the internal field can recover and approach the external applied field after few switching cycles. When this is considered in Fig. 8a, the space charge recombination will have the ability to keep the internal electric field level lower than the PDIV level at the negative-to-positive polarity reversal, thus no PD can be incepted at this time instant. Further, if the space charge field entirely vanishes before the transition from $0.5V_{dc}$ to V_{dc}, the internal field can exactly match the external applied field which is higher than the PDIV level at this time instant, thus PDs can be incepted as already obtained in Fig. 18a where few PDs are observed at the transition from 300V to 600V.

When power cables are used to supply the test sample with the generated 3L voltage waveform, the PD onset was recorded at 377V due to induced overvoltage oscillations. In this case, the peak sample voltage is 565 V (i.e., $1.5V_{dc}$). Fig. 18b shows the PD distribution in this scenario at 600V where several PDs are detected at the same phase locations predicted in the field change diagram previously shown in Fig. 8b.

The effectiveness of the Q3L PWM waveform is manifested when power cables are used, as it has the privilege of limiting the resultant overvoltage oscillations within 20% of the inverter rated voltage. When the Q3L waveform was applied to the test sample through the power cables, the PD onset has been recorded at 500V. Fig. 19a shows the

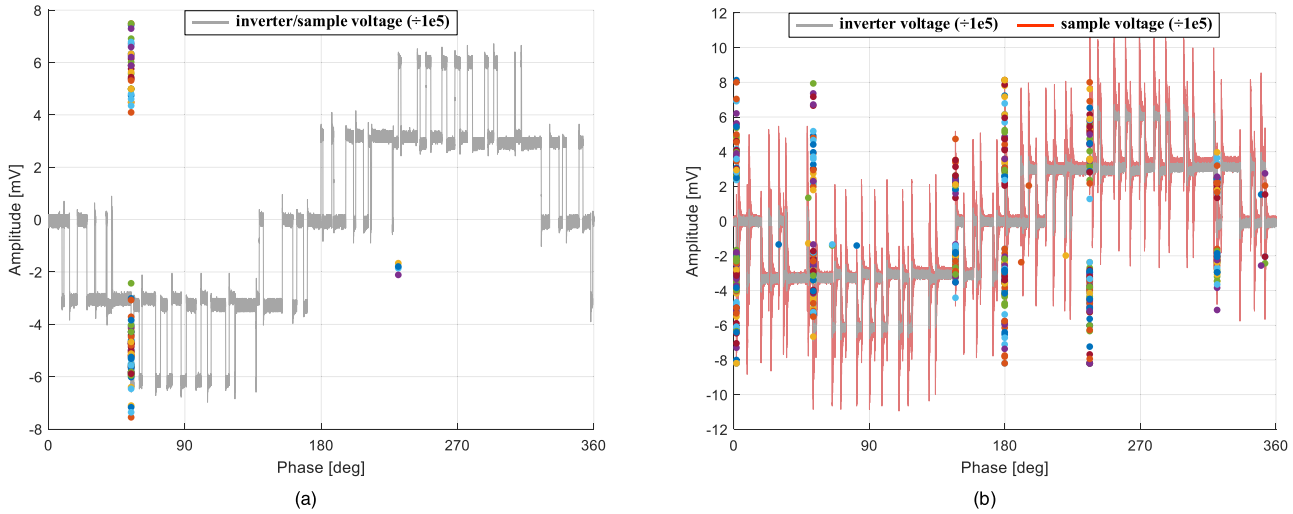

FIGURE 18. PRPD patterns for 3L PWM voltage waveform at 600V (a) without cable connection (b) with cable connection.

TABLE 2. Summary of experimental PD data.

	Unipolar 2L		Bipolar 2L		3L		Q3L
Use of power cables with critical length	×	✓	×	✓	×	✓	✓
DC-link voltage at which PD initiates	470V	300V	490V	187V	480V	377V	500V
Peak sample voltage at which PD initiates (PDIV)	470V	600V	490V	561V	480V	565V	600V
Minimum, maximum, and average PDs per fundamental cycle	{1, 2, 1.31}	{16, 34, 23.77}	{3, 15, 9.22}	{38, 40, 39.51}	{0, 2, 1.07}	{2, 8, 5.25}	{0, 3, 1.59}
High-dense PD locations within the fundamental cycle	Polarity reversal	All voltage flanks	Most of voltage flanks	All voltage flanks	Transition from $-0.5V_{dc}$ to $-V_{dc}$	- Polarity reversal - Transitions between $\pm 0.5V_{dc}$ and $\pm V_{dc}$ - Transitions between 0 and $\pm 0.5V_{dc}$	Polarity reversal

PD distribution in the fundamental cycle of the Q3L PWM waveform at 600V. Since the sample voltage has a unipolar 2L waveform, the PD distribution is comparable to that obtained in Fig. 16a. That is, many PD events are concentrated at the polarity reversal instants while very few PD events spread at other voltage transitions within the fundamental cycle. Figs. 19b and 19c show zoomed-in views for the rising and falling transitions, respectively, of the inverter and sample voltages. As can be noticed, the inverter voltage has a Q3L waveform while the sample voltage has a 2L waveform crossing the inverter voltage at the dwell time midway.

It is worth noting that, in some PRPD patterns, the number of observed PDs during the positive half cycle is less than that observed during the negative half cycle. Since the test sample is asymmetrical where a twisted pair of coated and uncoated magnet wires is used to reduce the insulation strength, there is an increased availability of electrodes form the uncoated wire, compared to the coated one, when the applied voltage is negative. This likely results in asymmetrical PD distribution, in amplitude and repetition rate, among the positive and negative half cycles of the applied voltage waveform [25].

Table 2 summarizes the experimental PD data obtained for the employed PWM voltage waveforms at the different operating scenarios. The dc-link voltage at which the PD onset was recorded is listed for each PWM waveform along with the corresponding peak sample voltage which represents the PDIV level. The minimum, maximum, and average number of detected PDs within the fundamental cycle (during 100 cycles) is tabulated to assess the dense of PD activities for the different PWM waveforms. The location of experimentally detected high-dense PDs are also presented.

VI. REMARKS

The focus of this article is to illustrate the PD inception mechanism for power electronics researchers and engineers to predict the number and location of probable PDs in winding insulation of inverter-fed motors for a given PWM voltage waveform. This has been experimentally verified on a twisted pair of magnet wires by generating PRPD patterns that show the PD number and location relative to the switching transitions of the applied voltage waveform. It should be noted that the twisted pair sample disregards the actual voltage distribution across the motor winding turns and the stator neutral point voltage fluctuation. However, the voltage at the terminals of the twisted pair sample impartially emulates the terminal voltage of an actual motor with reasonable representation of PD behavior in the motor turn-to-turn insulation system due to voltage surges that result from fast-switched PWM voltage pulses or consequent overvoltage stress when power cables are used. If an actual motor is used in the

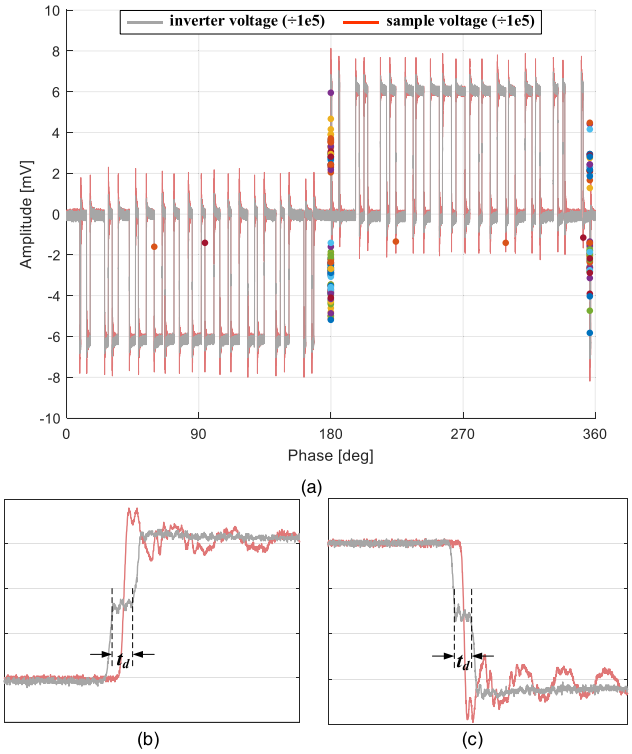

FIGURE 19. Inverter and sample voltages under Q3L PWM voltage waveform at $t_d = 140$ns (a) PRPD pattern at 600V with cable connection, (b) zoomed view at a rising voltage transition, and (c) zoomed view at a falling voltage transition.

experiment, there are several sources of PDs across different motor insulation systems (turn-to-turn, turn-to-ground, stator neutral-to-ground) [26]. With these mixed PD sources, it is difficult to distinguish and locate each specific PD event to the corresponding switching transition of the applied voltage waveform especially if the three phases of the motor are excited, in which case the PRPD patterns cannot be realized. Moreover, there is a difficulty in fitting the PD detection device inside/outside the motor to accurately measure the PD events in the motor winding insulation.

Several approaches can be adopted to reduce the likelihood of PD occurrence in inverter-fed motors. Among them, the utilization of passive filter networks [27] and soft-switching techniques [28] alleviates the dv/dt of switching transitions, which mitigates the motor overvoltage and reduces the uneven voltage distribution across the motor winding turns. Based on the analysis provided in this article, there are specific switching transitions in the fundamental cycle of the PWM voltage waveform at which the PD likelihood/magnitude is high (e.g., polarity reversal instants). Increasing the switching rise time at these specific switching instants can also reduce the dv/dt and accordingly the PD magnitude. This can be realized by employing smart gate driver circuits to drive the inverter switching devices with variable gate resistance that varies according to the PWM switching transitions, without compromising the switching power loss. On the other side, alternative insulating materials (e.g., corona resistant polyimide wire insulation) can be utilized to withstand higher stress levels which enhances the insulation endurance.

VII. CONCLUSION

This article has analyzed the PD behavior in inverter-fed motor drives from a power electronics point of view. Since inverter-fed motors are powered by PWM voltage waveforms with different characteristics depending on the adopted power converter topology and the applied modulation scheme, the PD activity in inverter-fed motors should be investigated within the fundamental cycle of the applied voltage waveform rather than under just few repetitive impulsive voltages. The attributes of the applied PWM waveform substantially impact the PD intensity and phase location that can be predicted by studying the aggregated electric field distribution associated with the PWM voltage waveform.

Four typical PWM voltage waveforms applicable to inverter-fed motor drives have been analyzed in this article to assess their PD behavior under steep-fronted voltage surges. It has been found that the voltage jump of the PWM waveform and consequent overvoltage is the dominant parameter governing the PD inception. The bipolar 2L waveform is severely vulnerable to high-dense PD activity due to the high voltage jump in each switching transition. The unipolar 2L waveform has a lower-dense PD activity, compared to the bipolar 2L waveform, since the voltage jump is halved. The 3L and Q3L waveforms have the lowest PD activity since the former is synthesized by reduced voltage steps while the latter has minimal overvoltage oscillations.

The impact of the PWM voltage waveform on PD behavior has been experimentally verified where PD data have been collected at different operating scenarios to generate statistical PRPD patterns. Although the PD process is stochastic, the theoretical analysis and experimental results are shown to be in a good agreement.

With the wider-adoption of fast-switching wide-bandgap devices and their applications in more-/all-electric aircrafts, where the low ambient pressure leads to more likelihood of PD across insulations, this article can be a very useful and timely reference for understanding the PD issues and finding appropriate mitigation measures.

REFERENCES

[1] P. Wheeler, "Technology for the more and all electric aircraft of the future," in *Proc. IEEE Int. Conf. Automatica (ICA-ACCA)*, Curico, Chile, Oct. 2016, pp. 1–5.

[2] P. Shamsi, M. McDonough, and B. Fahimi, "Wide-bandgap semiconductor technology: Its impact on the electrification of the transportation industry," *IEEE Electrific. Mag.*, vol. 1, no. 2, pp. 59–63, Dec. 2013.

[3] S. Yin, K. J. Tseng, R. Simanjorang, Y. Liu, and J. Pou, "A 50-kW high-frequency and high-efficiency SiC voltage source inverter for more electric aircraft," *IEEE Trans. Ind. Electron.*, vol. 64, no. 11, pp. 9124–9134, Nov. 2017.

[4] J. L. Guardado and K. J. Cornick, "The effect of coil parameters on the distribution of steep-fronted surges in machine windings," *IEEE Trans. Energy Convers.*, vol. 7, no. 3, pp. 552–559, Sep. 1992.

[5] M. J. Melfi, "Low-voltage PWM inverter-fed motor insulation issues," *IEEE Trans. Ind. Appl.*, vol. 42, no. 1, pp. 128–133, Jan. 2006.
[6] D. Leggate, J. Pankau, D. W. Schlegel, R. J. Kerkman, and G. L. Skibinski, "Reflected waves and their associated current [in IGBT VSIs]," *IEEE Trans. Ind. Appl.*, vol. 35, no. 6, pp. 1383–1392, Nov. 1999.
[7] W. Yin, "Failure mechanism of winding insulations in inverter-fed motors," *IEEE Elect. Insul. Mag.*, vol. 13, no. 6, pp. 18–23, Nov. 1997.
[8] G. Stone, S. Campbell, and S. Tetreault, "Inverter-fed drives: Which motor stators are at risk?" *IEEE Ind. Appl. Mag.*, vol. 6, no. 5, pp. 17–22, Sep. 2000.
[9] P. Wang, A. Cavallini, G. C. Montanari, and G. Wu, "Effect of rise time on PD pulse features under repetitive square wave voltages," *IEEE Trans. Dielectr. Electr. Insul.*, vol. 20, no. 1, pp. 245–254, Feb. 2013.
[10] P. Wang, A. Cavallini, and G. C. Montanari, "The influence of repetitive square wave voltage parameters on enameled wire endurance," *IEEE Trans. Dielectr. Electr. Insul.*, vol. 21, no. 3, pp. 1276–1284, Jun. 2014.
[11] P. Wang, H. Xu, J. Wang, W. Wang, and A. Cavallini, "Effect of repetitive impulsive voltage duty cycle on partial discharge features and insulation endurance of enameled wires for inverter-fed low voltage machines," *IEEE Trans. Dielectr. Electr. Insul.*, vol. 24, no. 4, pp. 2123–2131, Sep. 2017.
[12] P. Wang, A. Cavallini, and G. C. Montanari, "Characteristics of PD under square wave voltages and their influence on motor insulation endurance," *IEEE Trans. Dielectr. Electr. Insul.*, vol. 22, no. 6, pp. 3079–3086, Dec. 2015.
[13] L. Lusuardi, A. Rumi, A. Cavallini, D. Barater, and S. Nuzzo, "Partial discharge phenomena in electrical machines for the more electrical aircraft. Part II: Impact of reduced pressures and wide bandgap devices," *IEEE Access*, vol. 9, pp. 27485–27495, 2021.
[14] M. S. Diab, W. Zhou, C. Emersic, X. Yuan, and I. Cotton, "Impact of PWM waveforms on partial discharge in SiC-based motor drives," in *Proc. 47th Annu. Conf. IEEE Ind. Electron. Soc. (IECON)*, Oct. 2021, pp. 1–7.
[15] D. Cittanti, M. Guacci, S. Miric, R. Bojoi, and J. W. Kolar, "Comparative evaluation of 800 V DC-link three-phase two/three-level SiC inverter concepts for next-generation variable speed drives," in *Proc. 23rd Int. Conf. Electr. Mach. Syst. (ICEMS)*, Hamamatsu, Japan, Nov. 2020, pp. 1699–1704.
[16] M. J. Scott, J. Brockman, B. Hu, L. Fu, L. Xu, J. Wang, and R. Darbali Zamora, "Reflected wave phenomenon in motor drive systems using wide bandgap devices," in *Proc. IEEE Workshop Wide Bandgap Power Devices Appl.*, Knoxville, TN, USA, Oct. 2014, pp. 164–168.
[17] M. Schweizer, I. Lizama, T. Friedli, and J. W. Kolar, "Comparison of the chip area usage of 2-level and 3-level voltage source converter topologies," in *Proc. 36th Annu. Conf. IEEE Ind. Electron. Soc. (IECON)*, Glendale, AZ, USA, Nov. 2010, pp. 391–396.
[18] S. Lee and K. Nam, "An overvoltage suppression scheme for AC motor drives using a half DC-link voltage level at each PWM transition," *IEEE Trans. Ind. Electron.*, vol. 49, no. 3, pp. 549–557, Jun. 2002.
[19] M. S. Diab and X. Yuan, "A quasi-three-level PWM scheme to combat motor overvoltage in SiC-based single-phase drives," *IEEE Trans. Power Electron.*, vol. 35, no. 12, pp. 12639–12645, Dec. 2020.
[20] D. Fabiani, A. Cavallini, O. Mazzanti, and G. C. Montanari, "The effect of charge mobility on partial discharge characteristics of enamelled wires for PWM-controlled motors," in *Proc. IEEE Int. Conf. Solid Dielectr. (ICSD)*, Toulouse, France, Jul. 2004, pp. 856–859.
[21] A. Cavallini and G. C. Montanari, "Effect of supply voltage frequency on testing of insulation system," *IEEE Trans. Dielectrics Electr. Insul.*, vol. 13, no. 1, pp. 111–121, Feb. 2006.
[22] B. A. Fruth and D. W. Gross, "Phase resolving partial discharge pattern acquisition and frequency spectrum analysis," in *Proc. 4th Int. Conf. Properties Appl. Dielectric Mater. (ICPADM)*, Brisbane, QLD, Australia, Jul. 1994, pp. 578–581.
[23] C. Abadie, T. Billard, and T. Lebey, "Numerical signal processing methods for partial discharge detection in more electrical aircraft," in *Proc. IEEE Int. Conf. Dielectrics (ICD)*, Montpellier, France, Jul. 2016, pp. 540–543.
[24] L. Hao, P. L. Lewin, and J. A. Hunter, "Discrimination of multiple PD sources using wavelet decomposition and principal component analysis," *IEEE Trans. Dielectr. Electr. Insul.*, vol. 18, no. 5, pp. 1702–1711, Oct. 2011.
[25] H. Illias, T. Soon Yuan, A. H. A. Bakar, H. Mokhlis, G. Chen, and P. L. Lewin, "Partial discharge patterns in high voltage insulation," in *Proc. IEEE Int. Conf. Power Energy (PECon)*, Kota Kinabalu, Malaysia, Dec. 2012, pp. 750–755.
[26] Y. Xu, X. Yuan, F. Ye, Z. Wang, Y. Zhang, M. Diab, and W. Zhou, "Impact of high switching speed and high switching frequency of wide-bandgap motor drives on electric machines," *IEEE Access*, vol. 9, pp. 82866–82880, 2021.
[27] M. Pastura, S. Nuzzo, M. Kohler, and D. Barater, "Dv/Dt filtering techniques for electric drives: Review and challenges," in *Proc. 45th Annu. Conf. IEEE Ind. Electron. Soc. (IECON)*, Oct. 2019, pp. 7088–7093.
[28] W. Zhou, M. S. Diab, and X. Yuan, "Mitigation of motor overvoltage in SiC-device-based drives using a soft-switching inverter," in *Proc. IEEE Energy Convers. Congr. Expo. (ECCE)*, Oct. 2020, pp. 662–669.

MOHAMED DIAB (Senior Member, IEEE) received the B.Sc. (Hons.) and M.Sc. degrees in electrical engineering from Alexandria University, Egypt, in 2012, and 2015, respectively, and the Ph.D. degree in electrical engineering from the University of Strathclyde, Glasgow, U.K., in 2019. He is currently a Lecturer in power electronics with the School of Mechanical, Electrical and Manufacturing Engineering, Loughborough University, Loughborough, U.K. Prior to his current position, he was a Research Associate with the Electrical Energy Management Group, Department of Electrical and Electronic Engineering, University of Bristol, U.K. His research interests include applications of wide-bandgap devices, electric motor drives, high-power electronic converters, and renewable energy conversion systems.

WENZHI ZHOU (Graduate Student Member, IEEE) received the B.Sc. degree in electrical engineering from Dalian Jiaotong University, Dalian, China, in 2013, and the M.Sc. degree in electrical engineering from Zhejiang University, Hangzhou, China, in 2016. He is currently pursuing the Ph.D. degree with the Electrical Energy Management Group, Department of Electrical and Electronic Engineering, University of Bristol, Bristol, U.K. His research interests include wide-bandgap device applications, soft-switching, and partial discharge and motor drives.

CHRISTOPHER EMERSIC received the M.Phys. degree (Hons.) from The University of Manchester Institute of Science and Technology (UMIST), U.K., in 2003, and the Ph.D. degree from The University of Manchester, U.K., in 2006. He has worked as a Researcher with the University of Oklahoma, USA, and New Mexico Tech, USA. He is currently a Research Associate with The University of Manchester. His research interests include high voltage aerospace, partial discharge, thunderstorm electrification, atmospheric electricity, and cloud physics.

XIBO YUAN (Senior Member, IEEE) received the B.S. degree in electrical engineering from the China University of Mining and Technology, Xuzhou, China, in 2005, and the Ph.D. degree in electrical engineering from Tsinghua University, Beijing, China, in 2010. Since 2017, he has been a Professor with the Electrical Energy Management Group, Department of Electrical and Electronic Engineering, University of Bristol, Bristol, U.K. His research interests include power electronics and motor drives, wind power generation, multilevel converters, application of wide-bandgap devices, electric vehicles, and more electric aircraft technologies. He also holds the Royal Academy of Engineering/Safran Chair in Advanced Aircraft Power Generation Systems. He is currently the Director of the U.K. National Centre for Power Electronics and an Executive Committee Member of the IET Power Electronics, Machines and Drives (PEMD) network. He is also an Associate Editor of IEEE TRANSACTIONS ON INDUSTRY APPLICATIONS and IEEE JOURNAL OF EMERGING AND SELECTED TOPICS IN POWER ELECTRONICS. He is also a fellow of IET and received The Isao Takahashi Power Electronics Award, in 2018.

IAN COTTON (Senior Member, IEEE) received the B.Eng. degree (Hons.) in electrical engineering from the University of Sheffield, Sheffield, U.K., in 1995, and the Ph.D. degree in electrical engineering from The University of Manchester Institute of Technology (UMIST), Manchester, U.K., in 1998. He is currently a Professor in high voltage technology with The University of Manchester and the Joint Head of Research with the School of Engineering. His research work is based in the high voltage laboratories of the university and he is involved in work relating to power system equipment used in both terrestrial power and transportation systems.